Facile synthesis of MnO/carbon composites by a single-step nitrate-cellulose combustion synthesis for Li ion battery anode

Chunyu ZHU* [a], Cheng-gong Han [a], Genki Saito [a], and Tomohiro AKIYAMA

Faculty of Engineering, Hokkaido University, Sapporo 060-8628, Japan.
Corresponding author: chunyu6zhu@gmail.com and *chunyu6zhu@eng.hokudai.ac.jp*

Abstract

In this paper, a novel method is proposed to produce MnO/carbon composites, in which the MnO nanoparticles were embedded into a porous carbon matrix, by a single-step nitrate-cellulose combustion synthesis. The composition, structure and morphology of the composites were characterized by X-ray diffraction, Raman spectroscopy, X-ray photoelectron spectroscopy, thermogravimetric analysis, and scanning/transmission electron microscopy. The composites were used as lithium ion battery anodes to evaluate their electrochemical properties. The MnO/carbon composite with a proper carbon content showed enhanced cycling performance and capacity retention, which delivered a reversible capacity of 561 mAh g^{-1} after 90 cycles at 0.2 A g^{-1}. The easy production and good electrochemical properties enables the composite to be a possible candidate as an anode alternative for high-performance lithium ion battery.

Keywords: Li ion battery, anode, MnO, composite, cellulose, combustion synthesis

1. Introduction

Lithium ion batteries (LIBs) have been considered as one of the most promising power sources for application in mobile electronic devices and electric vehicles (EVs) because of their attractive high energy density and long life span. [1, 2] On the basis of a unique conversion reaction mechanism and high theoretical capacities (> 700 mA h g^{-1}), transition metal oxides (MO_x, M = Fe, Mn, Co, Ni, Cu, etc.) have been investigated as improved negative materials to substitute commercial graphite. Among various transition metal oxides, manganese monoxide (MnO) is an attractive anode material which shows advantages such as high theoretical capacity (755.6 mAh g^{-1}), low cost, environmental benignity, and abundant resources of manganese. However, practical application of pure MnO is still limited due to its low rate capability arising from the poor electrical conductivity and rapid capacity fading because of severe particle agglomeration and drastic volume changes over cycling.[3-10] To date, a number of efforts have been devoted to solve these problems. One effective strategy is to synthesize nanosized MnO, such as nanoparticles [11] and porous nanoflakes [12], to shorten the diffusion distance for electrons and lithium ions. Another efficient strategy is to construct nanocomposites with carbon materials such as carbon nanotube [13], carbon nanofiber [14, 15], and graphene [16, 17], which act as both a volume buffer to absorb the internal stress and a conductive network to increase electron and ion transport in the electrode.

To produce a carbon related composite, most of the carbon sources are derived from fossil fuel precursors such as coal, petroleum and natural gas, which are non-renewable resources. Cellulose is one of the most abundant and sustainable biomass materials in nature, which is an important structural component of the primary cell wall of green plants such as cotton and wood, making it a promising raw material for the fabrication of carbon related materials. [18-20] Combustion synthesis (CS) is a low-cost and energy-efficient method to prepare a broad range of materials such as ceramics, intermetallics and composites. CS is based on a highly exothermic, self-sustaining reaction generated by heating/igniting a redox mixture of oxidant and reductant.[21-24] Among various kinds of CS, solution combustion synthesis (SCS) is performed by heating a solution mixture of aqueous metal nitrates and organic fuels. Oxidizers are selected from metal nitrates since nitrates are water soluble and efficient oxidizers, whereas the fuel is ideally a substance containing carboxylic and amine groups such as urea, glycine, and hydrazides.[23-28] Cellulose is a kind of polysaccharide, which has a distinctive fiber morphology. In addition, cellulose is composed of microfibrils, which are 10-30 nm in width and have a surface area of 30-55 m^2 g^{-1}, making it a good absorbent for metal salts.[19, 29] Therefore, cellulose can be used as a solid fuel with absorption of metal nitrates to initiate a

combustion synthesis similar to SCS.

In this study, we present a facile one-step cellulose-based combustion synthesis method to directly produce MnO nanoparticles that are incorporated in porous carbon matrix. This synthesis route is suitable for large-scale production and the obtained samples exhibit enhanced electrochemical performance.

2. Experimental

In the experiment, 5, 7.5, and 10 mmol manganese nitrate were dissolved in 6 ml distilled water to form homogenous solutions, respectively. The above solutions were absorbed with 1 g commercially available dewaxed cottons, respectively. Subsequently, the wet cottons were dried at 70 ^{o}C. The dried samples were heated in a vertical tube reactor to 400 ^{o}C at a heating rate of 10 ^{o}C min^{-1} under Ar flow. A vigorous combustion reaction was observed at around 300 ^{o}C with the release of a large amount gases. After cooling, the samples were pulverized using a mortar-pestle. The samples were named as Mn5, Mn7.5, and Mn10, respectively, based on the amount of manganese nitrate.

The obtained samples were characterized by X-ray diffraction (XRD, Rigaku Miniflex, CuKα), transmission electron microscopy (TEM, 200 kV, JEM-2010F), and scanning electron microscopy (SEM, JEOL, JSM-7400F) for their structural and morphology analysis. A thermogravimetric (TG, Mettler Toledo) analyzer was used to determine the carbon content of the product. Raman spectra of the samples were acquired from a RENISHAW Raman spectrometer using an excitation wavelength of 532 nm. Surface functional groups and bonding characterization of the samples were performed on X-ray photoelectron spectroscopy (XPS, JEOL, JPS-9200) system using Mg-Kα X-ray source.

A two-electrode union-joint cell (a modified Swagelok cell) was used for the electrochemical test. [30, 31] The cell was assembled in an Ar-filled glove-box. The working electrode consisted of the active material, acetylene black conductive carbon, and polyvinylidene fluoride (PVDF) binder in a 80:10:10 weight ratio. A lithium disk was used as the reference and counter electrode, and a 1 M solution of $LiPF_6$ dissolved in a 50:50 (v/v) mixture of ethylene carbonate (EC) and dimethyl carbonate (DMC) was used as the electrolyte. Galvanostatic discharge/charge measurement was performed using an Arbin battery tester in a potential range of 3.0 and 0.01 V versus Li/Li^{+} at a constant temperature of 25 ºC. A potentiostat/galvanostat apparatus (Autolab, PGSTAT128N) was employed for cyclic voltammetry (CV) measurement at a potential scanning rate of 0.2 mV s^{-1} in a voltage range of 0-3.0 V.

3. Results and Discussion

3.1 Materials characterization

The phase, structure, and composition properties of the samples were characterized by XRD, Raman, and XPS techniques. Figure 1 shows the XRD patterns of the samples after a single step of combustion synthesis. All samples present a single phase of MnO (JCPDS no. 07-0230). The XRD peaks exhibit increasing intensity with the increasing amount of manganese precursor. Figure 2(a) exhibits the Raman spectra of the combustion synthesized samples. Peaks at about 650 cm^{-1} are observed in the spectra for all samples, which represent the existence of MnO. [13, 32, 33] The intensity of the MnO peak for sample Mn5 is greatly weaker than that for samples Mn7.5 and Mn10, indicating a lower content of MnO for sample Mn5. Two strong peaks at about 1350 and 1590 cm^{-1} are observed for all samples. This is assigned to the D-band and G-band, indicative of the disordered carbon and ordered graphitic carbon, respectively. The intensity ratio of the D-band to G-band for sample Mn5 is approximately 0.72, while the ratios for samples Mn7.5 and Mn10 are approximately 0.84. Here, a higher value of the intensity ratio of D-band to G-band indicates a higher disordering of the obtained carbon samples. XPS was also conducted to investigate the functional groups of the materials. The XPS survey spectra for the MnO/carbon composite, as shown in Figure 2(b), exhibit four peaks at 285.1, 530.9, 641.6, and 653.3 eV, corresponding to the C 1s, O 1s, Mn $2p_{3/2}$, and Mn $2p_{1/2}$, respectively.

The morphology and structural observation were further investigated using SEM and TEM. Figure 3 presents the SEM images of the combustion synthesized samples. Samples Mn10 and Mn7.5 are greatly pulverized, showing fine particles with diameters less than 1 μm. In contrast, sample Mn5 illustrates fine particles and a few large bulky micro-rods, indicative the shape of cotton fiber. Figure 4(a) exhibits the typical TEM image of sample Mn5. It is observed that sample Mn5 is porous, which contains macropores of around 50-300 nm. Figure 4(b) shows the typical selected area diffraction pattern for sample Mn5, which indicates a single phase of MnO. The high resolution TEM images are shown in Figures 4(c, d). It is observed that MnO nanocrystals of around 5 nm are embedded in the carbon matrix. The tap densities were measured to be 0.46, 0.38, and 0.31 g cm^{-3} for samples Mn10, Mn7.5, and Mn5, respectively.

The carbon contents of the synthesized samples were determined by TG analysis under air flow. The samples were heated to 800 °C at 10 °C min^{-1}. The TG profiles are presented in Figure 5. The MnO/carbon composites were oxidized to form Mn_2O_3 and CO_2 gas based on the following reactions:

$$MnO + 0.25\ O_2\ (g) = 0.5\ Mn_2O_3 \qquad (1)$$

$$C + O_2 (g) = CO_2 (g) \qquad (2)$$

Assuming that the carbon ratio in the composite is x (0 < x < 1), then the MnO ratio is (1-x). Therefore, we can obtain the following equation:

$$N = \frac{0.5 \times 157.87 \times (1-x)}{70.94} \qquad (3)$$

Here, N (0 < N < 1) is the weight of Mn_2O_3 after oxidation, i.e. the weight read from the TG scale at 800 °C; 157.87 is the molecular weight of Mn_2O_3 and 70.94 is the molecular weight of MnO. Therefore, the carbon contents x are calculated to be 49.73%, 30.55%, and 12.89% for samples Mn5, Mn7.5 and Mn10, respectively.

3.2 Electrochemical performance

The electrochemical properties of the synthesized samples were characterized by galvanostatic discharge/charge cycling test and CV measurement. The galvanostatic discharge/charge cycling was first tested at a constant current rate of 0.2 A g^{-1} with a voltage window of 3.0-0.01 V. Figure 6 shows the cycling performance for the three composite electrodes and their corresponding voltage profiles at 0.2 A g^{-1}. All capacities were calculated based on the weight of composites. In the first lithiation/delithiation cycles, the electrodes deliver lithiation/delithiation capacities of 1274.85/626.84, 1231.78/760.18, and 1144.34/681.25 mAh g^{-1} for samples Mn5, Mn7.5, and Mn10, respectively. The initial Coulombic efficiencies are calculated to be 49.17%, 61.71%, and 59.53% for these samples. The low Coulombic efficiency in the first cycle is caused by the irreversible capacity loss including the decomposition of electrolyte and the formation of surface electrolyte interface (SEI) layer.[34-36] However, from the second cycle, the efficiencies are increased to higher than 90% and stabilized at around 99% after a few cycles. The capacities for samples Mn7.5 and Mn10 show continuous decrease as cycle number, and after 90 cycles the discharge capacities are 345 and 258 mAh g^{-1}, respectively. In contrast, the cycling performance for sample Mn5 is the most stable; the discharge capacity is slightly decreased from 636 mAh g^{-1} at the 2nd cycle to 520 mAh g^{-1} at the 15th cycle and subsequently the capacity is increased and stabilized at around 565 mAh g^{-1}; after 90 cycles the discharge capacity is 561 mAh g^{-1} (173.91 mAh cm^{-3}). The greatly enhanced cycling performance for sample Mn5 is due to the adequate carbon matrix

which can effectively accommodate the volume change and reduce the aggregation of MnO nanoparticles during the charge/discharge process. Figures 6 (b, c, d) show the discharge-charge curves of the electrodes at 0.2 A g^{-1}. In the first discharge curves, the profiles show slopes from 2.0 V to 0.6 V, plateaus at around 0.3 V, and slopes from 0.3 V to 0.01 V. The plateaus represent the reduction of MnO to Mn, the slopes at 2.0 V to 0.6 V indicate the irreversible capacities which are mainly caused by the formation of SEI layer on the surface of electrode and the decomposition of the electrolyte, and the slopes at 0.3 V to 0.01 V represent the lithium insertion into carbon and the irreversible capacities caused by the formation of SEI layer as well. The length of the above slopes is greatly decreased from the second cycle. In the opposite charge process, slopes from 0.8 V to 1.5 V are observed, suggesting the oxidation of Mn to MnO. After the second cycle, the discharge-charge curves tend to overlap for sample Mn5, demonstrating a good cycling stability. In contrast, samples Mn7.5 and Mn10 show decreasing capacities as cycling.

The lithium insertion and extraction behavior of the electrodes are further investigated by CV measurement. The initial four cycles of CV curves at a scan rate of 0.2 mV s^{-1} are shown in Figure 7. Two cathodic peaks at around 0.1-0.2 V and 0.01 V are observed for all electrodes in the first cycle; the previous ones represent the reduction of MnO to Mn, and the latter ones are related to the lithium insertion into carbon materials and the formation of SEI layer and the decomposition of electrolyte. In the first charge process, anodic peaks at around 1.2 V are observed for all samples which are attributed to the oxidation of Mn to MnO. From the second cycle, the covered areas of CV curves are greatly reduced representing the capacity loss in the first cycles. After the second cycle, the CV curves tend to overlap, especially for sample Mn5, suggesting that these electrodes exhibit a gradually enhanced cycling stability for the Li insertion and extraction.

The rate capability for sample Mn5 is shown in Figure 8. As the current density increases from 0.1 to 0.2, 0.3, 0.4, 0.5, 0.7 and 1.0 A g^{-1}, the capacity decreases only slightly from 656 to 536, 491, 458, 441, 418 and 379 mAh g^{-1}, respectively. When the current density is reduced from 1.0 to 0.1 A g^{-1}, a capacity of 580 mAh g^{-1} can be recovered. The results indicate a good rate capability and a good structure stability of the MnO/carbon composite.

The enhanced lithium storage performance of the MnO/C composite could be attributed to the following aspects. First, the cotton-derived carbon matrix effectively enhances the electrical conductivity of MnO for the rapid electrochemical reactions, therefore leading to good rate capability. Secondly, the fine MnO nanocrystals as dispersed in carbon matrix provide short pathways for fast lithium ions insertion/extraction. Third, the porous structure could make a

good contact between the porous MnO/C composite and the electrolyte, and further facilitate the transportation of lithium ions. In addition, the porous structure could accommodate the volume changes during repeated lithiation/de-lithiation process. All of these contribute to the enhanced cyclability and rate capability of the MnO/C composite with a proper amount of carbon matrix.

4. Conclusion

In summary, MnO/carbon composites with different amounts of carbon were prepared by a single-step nitrate-cellulose combustion synthesis. The ultrafine MnO nanoparticles of about 5 nm were uniformly incorporated in the porous carbon matrix. This compositing structure and the strong synergistic effect between the MnO nanoparticles and the porous carbon matrix led to a high discharge capacity, a good cycling stability and enhanced rate performance for LIB anodes. The composite could deliver a specific capacity of 561 mAh g^{-1} after 90 cycles at a current density of 0.2 A g^{-1}. The greatly enhanced performance originates from the highly dispersed phase of MnO nanocrystals that provide the most active sites for lithium storage, and the continuous phase of the carbon matrix which acts as an electronic conduction network and a buffer to alleviate the volume change of MnO during cycling. The easy production and enhanced electrochemical properties of the composite indicate promising applications in high performance lithium ion batteries. The simple and cost-effective production approach could be extended to produce other metal oxides and carbon composites for versatile applications.

Acknowledgements

This work was supported by Yashima Environment Technology Foundation.

References

[1] B. Dunn, H. Kamath, J.-M. Tarascon, Electrical Energy Storage for the Grid: A Battery of Choices, Science, 334 (2011) 928-935.

[2] P. Roy, S.K. Srivastava, Nanostructured anode materials for lithium ion batteries, Journal of Materials Chemistry A, 3 (2015) 2454-2484.

[3] Y. Deng, L. Wan, Y. Xie, X. Qin, G. Chen, Recent advances in Mn-based oxides as anode materials for lithium ion batteries, RSC Advances, 4 (2014) 23914-23935.

[4] M.V. Reddy, G.V. Subba Rao, B.V.R. Chowdari, Metal Oxides and Oxysalts as Anode Materials for Li Ion Batteries, Chemical Reviews, 113 (2013) 5364-5457.

[5] Z. Cai, L. Xu, M. Yan, C. Han, L. He, K.M. Hercule, C. Niu, Z. Yuan, W. Xu, L. Qu, K. Zhao, L. Mai, Manganese Oxide/Carbon Yolk–Shell Nanorod Anodes for High Capacity Lithium Batteries, Nano Letters, 15 (2015) 738-744.

[6] J. Wang, C. Zhang, F. Kang, Nitrogen-Enriched Porous Carbon Coating for Manganese Oxide Nanostructures toward High-Performance Lithium-Ion Batteries, ACS Applied Materials & Interfaces, 7 (2015) 9185-9194.

[7] X. Gu, J. Yue, L. Chen, S. Liu, H. Xu, J. Yang, Y. Qian, X. Zhao, Coaxial MnO/N-doped carbon nanorods for advanced lithium-ion battery anodes, Journal of Materials Chemistry A, 3 (2015) 1037-1041.

[8] J.-G. Wang, C. Zhang, D. Jin, K. Xie, B. Wei, Synthesis of ultralong MnO/C coaxial nanowires as freestanding anodes for high-performance lithium ion batteries, Journal of Materials Chemistry A, 3 (2015) 13699-13705.

[9] H. Jiang, Y. Hu, S. Guo, C. Yan, P.S. Lee, C. Li, Rational Design of MnO/Carbon Nanopeapods with Internal Void Space for High-Rate and Long-Life Li-Ion Batteries, ACS Nano, 8 (2014) 6038-6046.

[10] J.-G. Wang, D. Jin, H. Liu, C. Zhang, R. Zhou, C. Shen, K. Xie, B. Wei, All-manganese-based Li-ion batteries with high rate capability and ultralong cycle life, Nano Energy, 22 (2016) 524-532.

[11] Y. Lu, L. Zhang, J. Li, Y.-D. Su, Y. Liu, Y.-J. Xu, L. Dong, H.-L. Gao, J. Lin, N. Man, P.-F. Wei, W.-P. Xu, S.-H. Yu, L.-P. Wen, MnO Nanocrystals: A Platform for Integration of MRI and Genuine Autophagy Induction for Chemotherapy, Advanced Functional Materials, 23 (2013) 1534-1546.

[12] X. Li, D. Li, L. Qiao, X. Wang, X. Sun, P. Wang, D. He, Interconnected porous MnO nanoflakes for high-performance lithium ion battery anodes, Journal of Materials Chemistry, 22 (2012) 9189-9194.

[13] Z. Yang, J. Lv, H. Pang, W. Yan, K. Qian, T. Guo, Z. Guo, Facile Synthesis of Coaxial CNTs/MnOx-Carbon Hybrid Nanofibers and Their Greatly Enhanced Lithium Storage Performance, Scientific Reports, 5 (2015) 17473.

[14] J.-G. Wang, Y. Yang, Z.-H. Huang, F. Kang, MnO-carbon hybrid nanofiber composites as superior anode materials for lithium-ion batteries, Electrochimica Acta, 170 (2015) 164-170.

[15] G. Zhang, H.B. Wu, H.E. Hoster, X.W. Lou, Strongly coupled carbon nanofiber-metal oxide coaxial

nanocables with enhanced lithium storage properties, Energy & Environmental Science, 7 (2014) 302-305.
[16] S.M. Lee, S.H. Choi, J.-K. Lee, Y.C. Kang, Electrochemical properties of graphene-MnO composite and hollow-structured MnO powders prepared by a simple one-pot spray pyrolysis process, Electrochimica Acta, 132 (2014) 441-447.
[17] J.-G. Wang, D. Jin, R. Zhou, X. Li, X.-r. Liu, C. Shen, K. Xie, B. Li, F. Kang, B. Wei, Highly Flexible Graphene/Mn3O4 Nanocomposite Membrane as Advanced Anodes for Li-Ion Batteries, ACS Nano, 10 (2016) 6227-6234.
[18] H. Bi, Z. Yin, X. Cao, X. Xie, C. Tan, X. Huang, B. Chen, F. Chen, Q. Yang, X. Bu, X. Lu, L. Sun, H. Zhang, Carbon Fiber Aerogel Made from Raw Cotton: A Novel, Efficient and Recyclable Sorbent for Oils and Organic Solvents, Advanced Materials, 25 (2013) 5916-5921.
[19] H. Birol, C. Renato Rambo, M. Guiotoku, D. Hotza, Preparation of ceramic nanoparticles via cellulose-assisted glycine nitrate process: a review, RSC Advances, 3 (2013) 2873-2884.
[20] C. Zhu, T. Akiyama, Cotton derived porous carbon via an MgO template method for high performance lithium ion battery anodes, Green Chemistry, 18 (2016) 2106-2114.
[21] K. Morsi, The diversity of combustion synthesis processing: a review, J. Mater. Sci., 47 (2012) 68-92.
[22] S.T. Aruna, A.S. Mukasyan, Combustion synthesis and nanomaterials, Current Opinion in Solid State and Materials Science, 12 (2008) 44-50.
[23] C. Zhu, C.-g. Han, T. Akiyama, Controlled synthesis of LiNi0.5Mn1.5O4 cathode materials with superior electrochemical performance through urea-based solution combustion synthesis, RSC Advances, 5 (2015) 49831-49837.
[24] C. Zhu, A. Nobuta, I. Nakatsugawa, T. Akiyama, Solution combustion synthesis of LaMO3 (M = Fe, Co, Mn) perovskite nanoparticles and the measurement of their electrocatalytic properties for air cathode, International Journal of Hydrogen Energy, 38 (2013) 13238-13248.
[25] A.S. Mukasyan, Solution Combustion as a Promising Method for the Synthesis of Nanomaterials, Advances in Science and Technology, 63 (2011) 187-196.
[26] K. Rajeshwar, N.R. de Tacconi, Solution combustion synthesis of oxide semiconductors for solar energy conversion and environmental remediation, Chemical Society Reviews, 38 (2009) 1984-1998.
[27] C. Zhu, A. Nobuta, G. Saito, I. Nakatsugawa, T. Akiyama, Solution combustion synthesis of LiMn2O4 fine powders for lithium ion batteries, Advanced Powder Technology, 25 (2014) 342-347.
[28] C. Zhu, T. Akiyama, Optimized conditions for glycine-nitrate-based solution combustion synthesis of LiNi0.5Mn1.5O4 as a high-voltage cathode material for lithium-ion batteries, Electrochimica Acta, 127 (2014) 290-298.
[29] B. Wang, R. Karthikeyan, X.-Y. Lu, J. Xuan, M.K.H. Leung, Hollow Carbon Fibers Derived from Natural Cotton as Effective Sorbents for Oil Spill Cleanup, Industrial & Engineering Chemistry Research,

52 (2013) 18251-18261.
[30] C. Zhu, G. Saito, T. Akiyama, Urchin-like hollow-structured cobalt oxides with excellent anode performance for lithium-ion batteries, Journal of Alloys and Compounds, 646 (2015) 639-646.
[31] C. Zhu, G. Saito, T. Akiyama, A facile solution combustion synthesis of nanosized amorphous iron oxide incorporated in a carbon matrix for use as a high-performance lithium ion battery anode material, Journal of Alloys and Compounds, 633 (2015) 424-429.
[32] C. Zhu, N. Sheng, T. Akiyama, MnO nanoparticles embedded in a carbon matrix for a high performance Li ion battery anode, RSC Advances, 5 (2015) 21066-21073.
[33] C. Yang, Q. Gao, W. Tian, Y. Tan, T. Zhang, K. Yang, L. Zhu, Superlow load of nanosized MnO on a porous carbon matrix from wood fibre with superior lithium ion storage performance, Journal of Materials Chemistry A, 2 (2014) 19975-19982.
[34] W. Zhu, H. Huang, W. Zhang, X. Tao, Y. Gan, Y. Xia, H. Yang, X. Guo, Synthesis of MnO/C composites derived from pollen template for advanced lithium-ion batteries, Electrochimica Acta, 152 (2015) 286-293.
[35] S. Wang, C. Xiao, Y. Xing, H. Xu, S. Zhang, Formation of a stable carbon framework in a MnO yolk-shell sphere to achieve exceptional performance for a Li-ion battery anode, Journal of Materials Chemistry A, 3 (2015) 15591-15597.
[36] H. Cao, X. Wang, H. Gu, J. Liu, L. Luan, W. Liu, Y. Wang, Z. Guo, Carbon coated manganese monoxide octahedron negative-electrode for lithium-ion batteries with enhanced performance, RSC Advances, 5 (2015) 34566-34571.

Figure 1. XRD pattern of the obtained products.

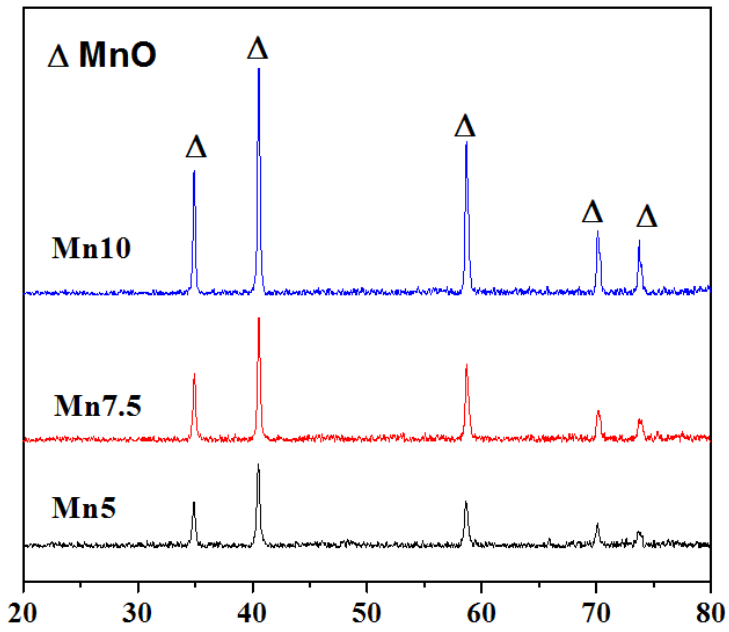

Figure 2. Raman spectra (a) and XPS spectra (b) of the obtained products.

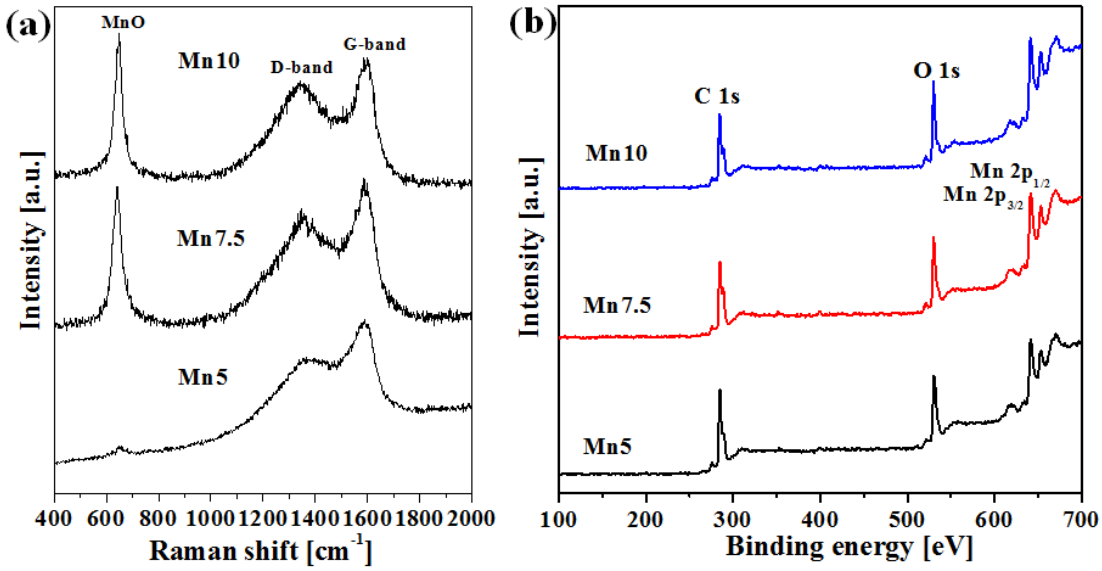

Figure 3. SEM images of the obtained products.

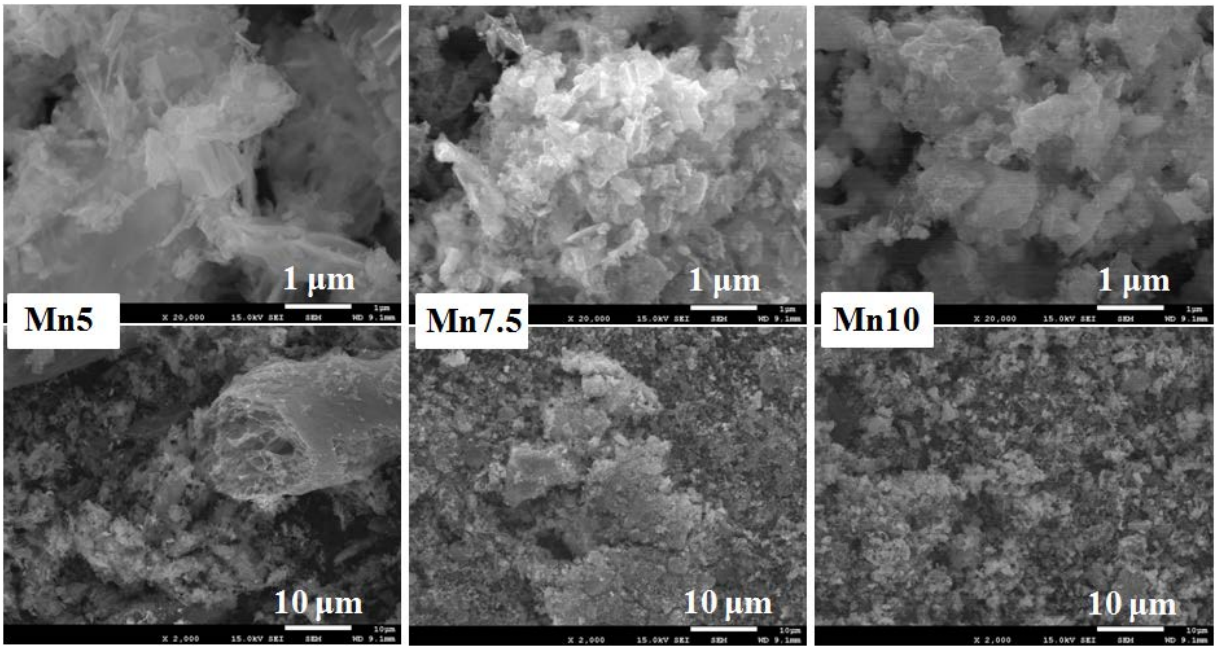

Figure 4. TEM observation results of sample Mn5. (a) A typical TEM image at a low magnification; (b) a typical selected area diffraction pattern; (c, d) high resolution TEM images.

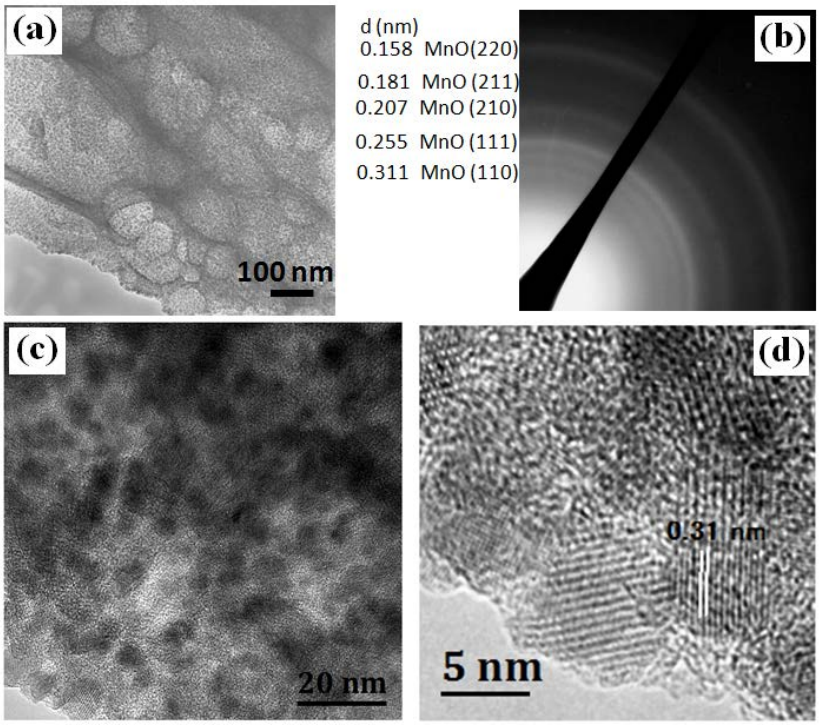

Figure 5. TG profiles of the samples under air flow.

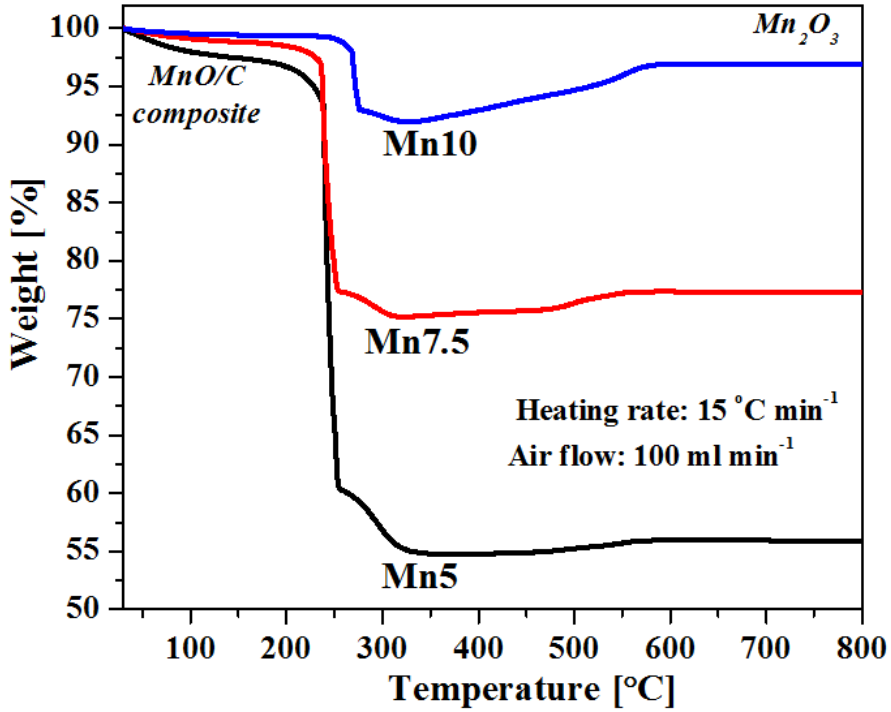

Figure 6. (a) Cycling performance of the as-prepared MnO/carbon composites at a current density of 0.2 A g^{-1}, and (b, c, d) the corresponding discharge-charge profiles.

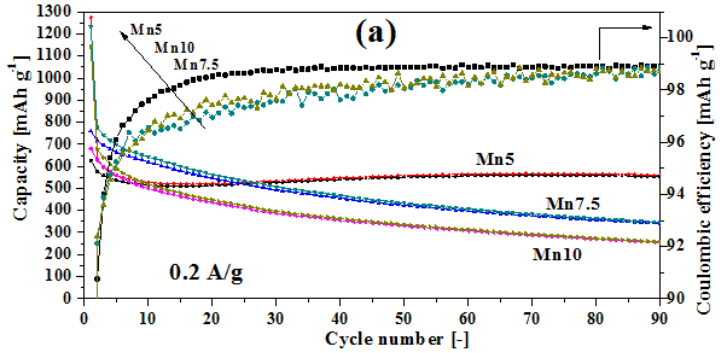

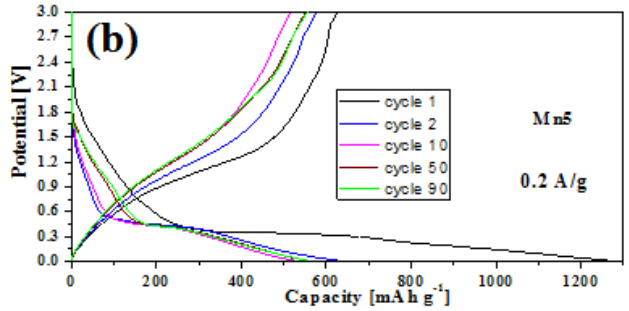

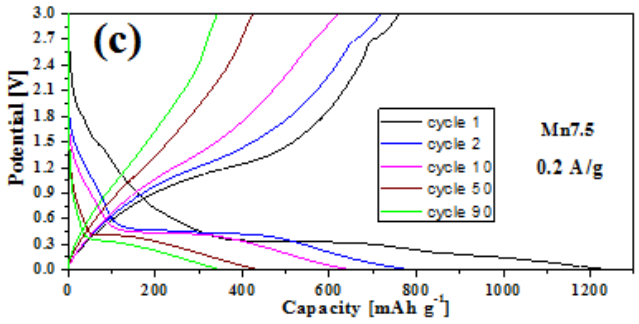

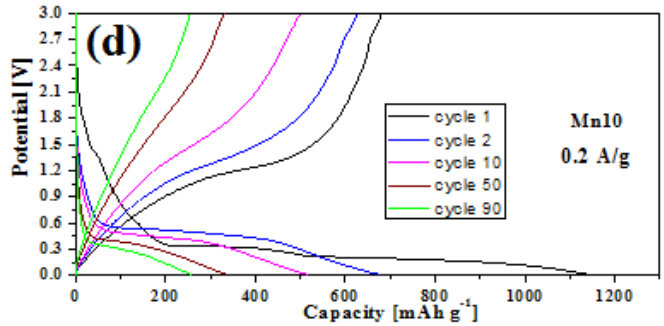

Figure 7. CV curves of the MnO/carbon composites at 0.2 mV s^{-1}.

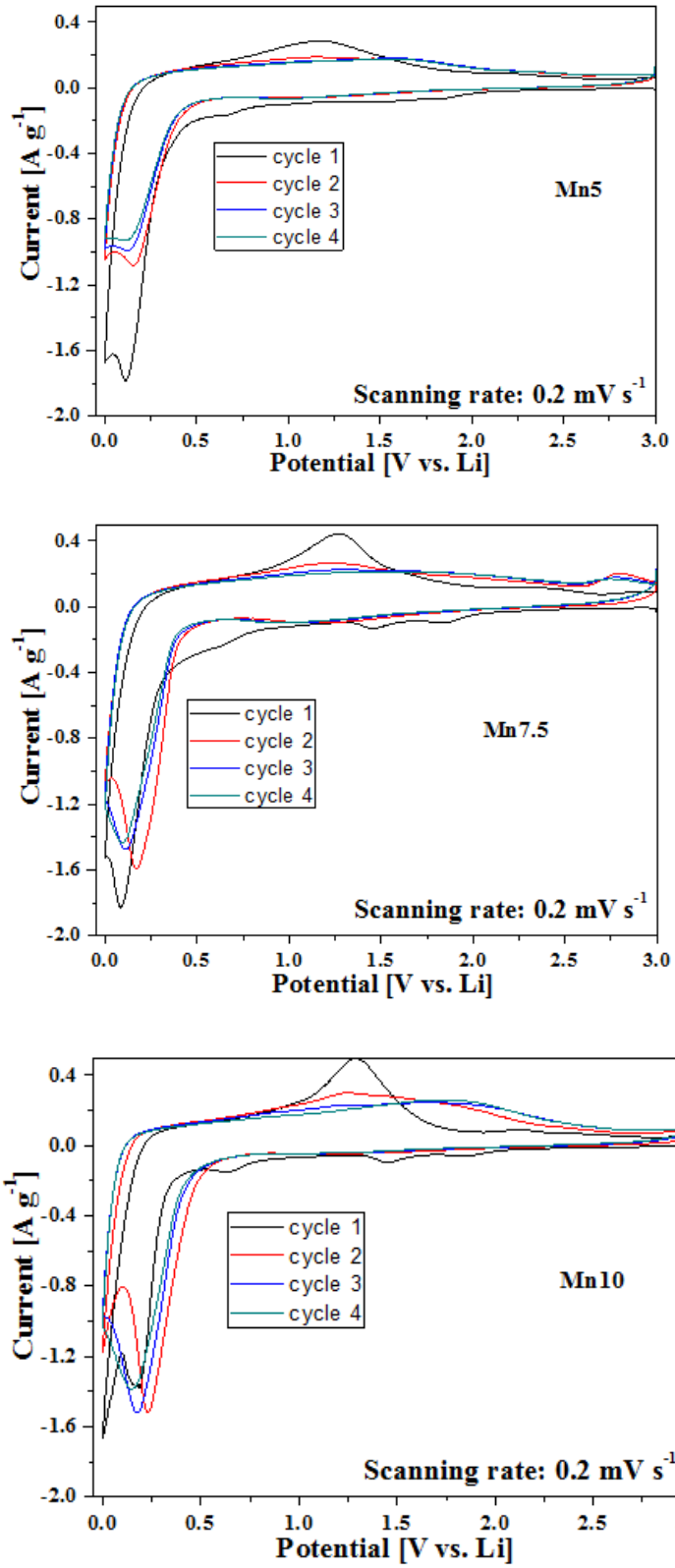

Figure 8. Rate capability test for MnO/carbon composite (Mn5) at various current densities.